Bottom-Up Synthesized Nanoporous Graphene Transistors

*Zafer Mutlu, Peter H. Jacobse, Ryan D. McCurdy, Juan P. Llinas, Yuxuan Lin, Gregory C. Veber, Felix R. Fischer, Michael F. Crommie, and Jeffrey Bokor**

Nanoporous graphene (NPG) can exhibit a uniform electronic band gap and rationally-engineered emergent electronic properties, promising for electronic devices such as field-effect transistors (FETs), when synthesized with atomic precision. Bottom-up, on-surface synthetic approaches developed for graphene nanoribbons (GNRs) now provide the necessary atomic precision in NPG formation to access these desirable properties. However, the potential of bottom-up synthesized NPG for electronic devices has remained largely unexplored to date. Here, FETs based on bottom-up synthesized chevron-type NPG (C-NPG), consisting of ordered arrays of nanopores defined by laterally connected chevron GNRs, are demonstrated. C-NPG FETs show excellent switching performance with on–off ratios exceeding 10^4, which are tightly linked to the structural quality of C-NPG. The devices operate as p-type transistors in the air, while n-type transport is observed when measured under vacuum, which is associated with reversible adsorption of gases or moisture. Theoretical analysis of charge transport in C-NPG is also performed through electronic structure and transport calculations, which reveal strong conductance anisotropy effects in C-NPG. The present study provides important insights into the design of high-performance graphene-based electronic devices where ballistic conductance and conduction anisotropy are achieved, which could be used in logic applications, and ultra-sensitive sensors for chemical or biological detection.

1. Introduction

Nanoporous graphene (NPG) materials have been widely studied and exploited for opening a band gap in bulk graphene while maintaining its high mobility, which is required for high-performance electronic devices such as field-effect transistors (FETs).[1] Experimental realization of NPG has so far been achieved almost exclusively by top-down lithography approaches.[1–3] These approaches inherently lack the ability to produce nanosize pores with atomic precision and, as a result, a technologically relevant uniform bandgap, which is a primary prerequisite for realizing large-scale, high mobility graphene-based electronics. Recent advancements in the bottom-up, on-surface synthesis of graphene nanoribbons (GNRs) have led to the development of atomically precise GNR-based NPGs with well-defined electronic properties, containing highly ordered arrays of structurally identical nanopores.[4–7] However, research on the electron transport properties of bottom-up synthesized NPG remains scarce.

Our group has recently demonstrated a highly scalable rational bottom-up approach for the on-surface synthesis of atomically precise chevron-type NPG (C-NPG), which consists of quasi 1D chevron-type GNRs (C-GNRs), decorated with five-membered rings, that have been laterally fused into an extended 2D structure.[6] C-NPG exhibits a uniform electronic band gap with localized frontier electronic states that are unattainable in either bulk graphene or top-down etched graphene nanomeshes. These states can serve as an addressable conduction pathway for semiconductor electronic devices. Thanks to the unique 2D network-like structure, C-NPG can overcome a number of materials science challenges plaguing

---

Z. Mutlu, J. P. Llinas, Y. Lin, J. Bokor
Department of Electrical Engineering and Computer Sciences
University of California
Berkeley, CA 94720, USA
E-mail: jbokor@berkeley.edu

Z. Mutlu, J. P. Llinas, Y. Lin
The Molecular Foundry
Lawrence Berkeley National Laboratory
Berkeley, CA 94720, USA

P. H. Jacobse, M. F. Crommie
Department of Physics
University of California
Berkeley, CA 94720, USA

R. D. McCurdy, G. C. Veber, F. R. Fischer
Department of Chemistry
University of California
Berkeley, CA 94720, USA

F. R. Fischer, M. F. Crommie, J. Bokor
Materials Sciences Division
Lawrence Berkeley National Laboratory
Berkeley, CA 94720, USA

F. R. Fischer, M. F. Crommie
Kavli Energy NanoSciences Institute at University of California
Berkeley and Lawrence Berkeley National Laboratory
Berkeley, CA 94720, USA

The ORCID identification number(s) for the author(s) of this article can be found under https://doi.org/10.1002/adfm.202103798.

DOI: 10.1002/adfm.202103798

the integration of bottom-up synthesized graphene nanomaterials in transistors, such as facilitating transfer onto dielectric surfaces with high-yield and realizing uniformity without suffering from lateral displacement and aggregation effects observed after transfer of 1D GNRs.[8–10] Furthermore, working device yield and performance may be enhanced by increasing conduction pathways. Despite the promise of bottom-up synthesized NPG materials, their application in FETs has not been fully exploited yet, in contrast to GNR FETs, which have seen significant progress.[7,10–18]

In this paper, we demonstrate short-channel FETs with bottom-up synthesized C-NPG and study their charge-transport characteristics both experimentally and theoretically. C-NPG was first synthesized on gold/mica substrates through a bottom-up, on-surface synthetic approach and then transferred on dielectric substrates using a wet transfer method for device integration.[6,12] A reliable ex situ Raman characterization protocol was developed for monitoring the quality and air stability of C-NPG grown on gold substrates throughout the fabrication process. Bottom-up synthesized C-NPG FETs were fabricated with high on–off ratios exceeding 10^4, which was found to strongly correlate with the structural quality of the material as inferred from scanning tunneling microscopy (STM) imaging characterization. Even though C-NPG is an NPG consisting of C-GNRs, the on–off ratio of bottom-up C-NPG FETs was found to outperform that of bulk graphene,[19] top-down graphene nanomeshes[1,2] and C-GNR[20–22] FETs (see Table S1, Supporting Information for a detailed comparison), proving that the bottom-up method gives access to materials that have superior characteristics by virtue of their tightly controlled structural and electronic properties. Additionally, it was found that air exposure has a reversible p-type doping effect on C-NPG FETs. Finally, we performed electronic structure and transport calculations which reveal strong conductance anisotropy effects in C-NPG and further underpin the quintessential role of the structural quality.

2. Results and Discussion

The first step in the fabrication of C-NPG FETs entails the bottom-up synthesis of C-NPG, using a standard surface-synthetic protocol consisting of thermally activated Ullmann coupling followed by graphitization of either dedicated molecular precursors **1** (methyl cross-linking handle) or **2** (fluorene cross-linking handle), as shown in **Figure 1**a.[6] The graphitization reactions include both intramolecular cyclodehydrogenation (CDH) and a cross-dehydrogenative coupling, the latter of which involves lateral fusion of nanoribbons forming rubicene-type interfaces. The rubicene interfaces give rise to an interesting, emergent in-gap band (IGB) of states, while the chevron backbone of the ribbons effectively dictates the formation of nanopores in the fused structure. The C-NPG structure is shown in Figure 1a, where the *x*-axis indicates the growth direction of the ribbons whereas the *y*-axis denotes the fusion direction. Subsequent strands may fuse in two different configurationally isomeric orientations relative to the previous strand, which we indicate as syn (the nanopore orientation remains the same) and anti (the nanopore orientation flips).

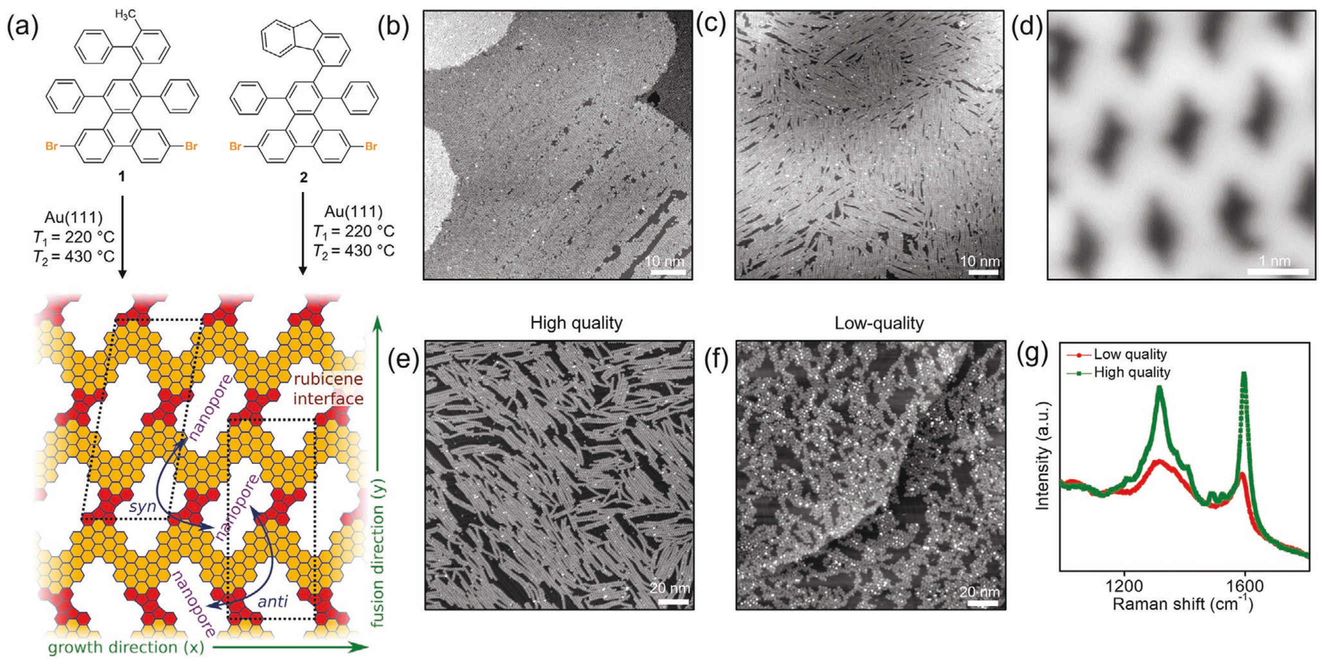

Figure 1. Growth and structural identification of C-NPG. a) Schematic representation of the bottom-up synthesis of C-NPG from molecular precursors **1** and **2**. The rubicene-type interface highlighted in red and the 2D syn and anti unit cells are indicated by dashed parallelograms. STM topographic image (V = −2 V; I = 20 pA) of a high-coverage monolayer C-NPG film from precursor **1** b) in the polymer phase and after (V = −2 V; I = 20 pA) c) CDH and cross-dehydrogenative coupling. d) High-resolution STM topographic image (V = 0.2 V; I = 50 pA) of the C-NPG film, revealing the nanopores. STM topographic images of two different low coverage monolayer C-NPG films of e) high-quality (V = −1.8 V; I = 20 pA) and f) low-quality (V = −2 V; I = 20 pA), respectively, obtained from precursors **1** and **2**. g) Raman spectra corresponding to the samples shown in (e) and (f).

Samples were prepared by deposition of molecular precursor **1** or **2** onto an Au(111)/mica substrate held at $T_1 = 220$ °C. Hot-substrate deposition leads to improved Ullmann coupling and long polymers since at any instance during the growth, the coverage of molecules is low and will therefore predominantly extend the polymers already present on the surface (Figure 1b). CDH and cross-dehydrogenative coupling occur simultaneously when the polymer film is subsequently annealed to $T_2 = 430$ °C, resulting in a monolayer C-NPG film (Figure 1c). At this stage, the polymer chains convert into C-GNRs that are concurrently fused through rubicene-type linkages, giving rise to the 2D nanoporous structure (Figure 1d). More STM topographic images of six different C-NPG samples with varying coverage obtained from precursors **1** and **2** during growth optimization experiments are given in Figures S1 and S2, Supporting Information, respectively, to demonstrate the scalability and controllability of our growth method.

We next demonstrate that Raman spectroscopy can be used to assess the quality of C-NPG in the context of long-range order and crystallinity. For this purpose, we grew two C-NPG samples of different quality at low-coverage, one with high-quality (Figure 1e) and one with low-quality (Figure 1f). While the high-quality sample consists of uniform long cross-linked C-NPG of up to ≈50 nm in the growth direction, which is locally aligned on the surface, the low-quality sample has several disordered small, interconnected patches randomly distributed on the surface. As shown in Figure 1g, Raman spectra recorded on the two samples reveal two fundamental peaks at ≈1596 and ≈1316 cm^{-1} that are referred to as G-like and D-like modes, respectively, in analogy with graphene (See Figure S3, Supporting Information for photoluminescent spectra taken from these two samples).[23,24] The related overtone and combination peaks also appear between ≈2500 and ≈3300 cm^{-1} (Figure S4, Supporting Information). Unlike graphene, for which the D band is activated only in the presence of defects, C-NPG shows a D peak even if it is defect-free, owing to its nanoporosity that is absent in pristine graphene.[23,24] The line width and relative intensity of the G and D peaks can be used as a reliable probe for the structural quality, along the lines of previous analyses of GNRs,[11] CNTs,[25] and graphene.[26] The Raman spectra of the high-quality sample show relatively higher intensity and narrower G and D peaks as well as a higher intensity ratio (>1) of the G to D peaks compared to the low-quality sample. In addition to the G and D peaks, there are several fine-structure peaks present at the low-energy side of the G band, as well as a series of peaks around the D band in the high-quality sample. Similar small Raman features were observed in both experimental and calculated Raman spectra of C-GNRs in previous studies, where these small features were attributed to the low dimensionality and high-quality.[21,22,27–33] Since C-NPG consists of C-GNRs, the appearance of these small Raman peaks is expected, and their presence after exposure to air even after several weeks (Figure S5, Supporting Information) strongly suggests that C-NPG is stable under ambient conditions.[15,34] The absence of the Raman peaks at ≈1640 and ≈1160 cm^{-1} in the spectra, which are assigned to the bending mode of the OH group, and the C—O stretching mode, respectively—also confirms the high oxidation stability of C-NPG.[34]

Furthermore, we demonstrate the fabrication of short-channel FETs with C-NPG as the active channel material. We fabricated devices with a local back gate geometry having a ≈8 nm thick W gate capped with a ≈5.5 nm HfO_2 gate dielectric and ≈12 nm Pd contacts, as shown schematically in **Figure 2**a. Local HfO_2 back gate has been proven to significantly improve the electrical performance of GNR[11,12] and CNT[35] FETs. C-NPG films were transferred from gold/mica substrates onto prepatterned device substrates using a wet-etch transfer method, which is commonly used in transferring GNRs from gold/mica substrates to insulator substrates.[9,13] Pd electrodes with a ≈20 nm channel length were then fabricated using electron beam lithography (EBL) (Figure 2c).

A representative scanning electron microscopy (SEM) image of a C-NPG film transferred onto a device substrate (Figure 2b) shows continuous film morphology without significant wrinkles, pinholes, or tears, apart from a few folded regions at the edges. Therefore, C-NPG is highly uniform on the scale of several micrometers (See also Figure S6, Supporting Information for Raman spectra collected from five different regions of the film, which further confirm the large-scale uniformity of C-NPG). The thickness of the C-NPG film as measured with atomic force microscopy (AFM) (inset of Figure 2b) is ≈2 nm, comparable to values reported for C-GNRs.[20,21] Consistent with the SEM result, high-resolution AFM (Figure S7, Supporting Information) of the C-NPG film reveals a 2D film-like morphology with a smooth surface, in contrast with GNRs, which are suspected to form aggregates during transfer.[9,10] Aggregation can cause increased device-to-device variation and degraded device performance due to ribbon-to-ribbon screening effects. In this regard, 2D CNPG may offer a significant advantage over GNRs as FET channel material.

Raman spectroscopy was used to verify the structural integrity of C-NPG after transfer onto the device substrate. A comparison of Raman spectra of C-NPG grown on gold and after transfer and device processing (Figure 2d) shows that all C-NPG peaks, including the fine features, are preserved. While this suggests that C-NPG films remain intact during the process without significant structural modification, the intensity of the overtone and combination peaks is increased, the G peak is upshifted, and the intensity ratio of the G and D peaks is slightly altered.[9] This can be attributed to the interaction with the substrate, but future work is needed to carefully determine whether any other factors, such as doping or functionalization, could also contribute to the changes in Raman spectra.[36]

Figure 2e shows the drain–source current-gate voltage (I_d–V_g) behavior at a fixed drain–source voltage bias (V_d) in air at room temperature for the FET device prepared from a high-quality C-NPG sample (Figure 1e), and a measurement on the device fabricated from a low-quality sample (Figure 1f), shown as comparison. The high-quality device exhibits a particularly high on–off ratio exceeding 10^4, which is significantly higher than the values reported for bulk graphene,[19] lithographically defined graphene nanomeshes,[2] and C-GNRs.[20–22] The minimum off-current can be attributed to gate leakage (Figure S8b, Supporting Information), and the noise in the current is likely due to rearrangement of surface charge traps in the substrate.[15] The devices without C-NPG channel material do not show any conduction (Figure S8a, Supporting Information),

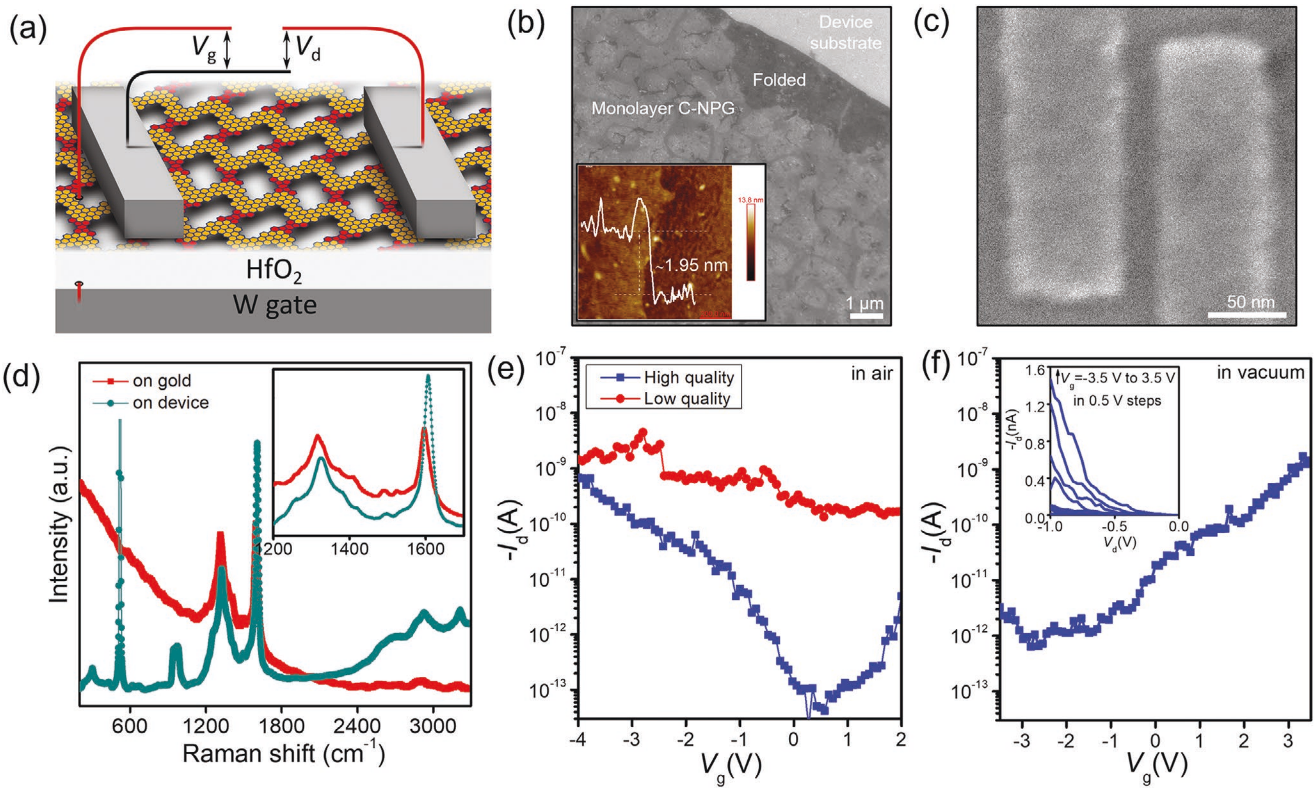

Figure 2. Device architecture, transfer, and electrical properties. a) Schematic of the device structure of a local back-gated C-NPG FET. b) Scanning electron microscopy (SEM) image of a C-NPG film after transferring onto a device substrate. The inset shows an atomic force microscopy (AFM) topographic image of the C-NPG film measured on a folded region, with a representative height profile indicated. c) SEM image of the C-NPG device after patterning of Pd contacts d) Raman spectra of as-grown C-NPG on gold and C-NPG after transfer and device processing. e) Room temperature I_d–V_g characteristics of the FET devices prepared from the high-quality and low-quality C-NPG samples (Figure 1e,f) measured at $V_d = -2$ V in air. f) Room temperature I_d–V_g characteristics of the high-quality C-NPG FET measured at $V_d = -1$ V under vacuum. The inset shows the I_d–V_d characteristics of the device. See Figure S9b, Supporting Information for the I_d–V_g characteristics of a low-quality C-NPG FET at $V_d = -1$ V in air and under vacuum.

and the gate leakage current of the devices is ≈2 orders of magnitude lower than the on-current (Figure S8b, Supporting Information), which substantiates that the observed characteristics originate purely from the C-NPG films. While both devices exhibit a similar on-current (in the nA range), the low-quality device exhibits a relatively high off-current, resulting in a lower on–off ratio of <10. The low on–off ratio is a known consequence of charge transport through a percolation network consisting of finite-sized patches that are interlinked.[14,18] These findings suggest that there is a strong correlation between the electrical performance and the structural quality of C-NPG.

C-NPG FETs were found to exhibit p-type conduction when measured in air, as the drain current increases with negative gate voltage (Figure 2e). p-type transport is also commonly reported in studies on GNR and CNT devices contacted with Pd metals, where it is usually attributed to the band alignments at the metal–semiconductor contacts or doping from environmental adsorbates.[13,37] Moreover, the devices switch to n-type conduction under vacuum (Figure 2f). A similar device behavior switch was also reported in our previous work on 7-AGNR FETs,[13] and in studies on the FETs based on CNTs[37] and 2D materials.[38] The switch from p-type to n-type transport under vacuum has previously been attributed to the displacement of molecular adsorbates[13] and/or the removal of dopants suppressing electron conduction.[13,37] Given that a similar effect has been observed in related systems, we believe that the p-type doping effect in air also originates from the Fermi-level shift induced by molecular adsorbates, rather than a change in the electronic structure. Although the structure is air stable (Figure S5, Supporting Information) and preserved after transfer and device processing (Figure 2d), owing to its nanoporosity, C-NPG might be particularly sensitive to molecular absorbates introduced during air exposure, transfer, and/or device fabrication. Indeed, the recovery of p-type transport behavior after air exposure (Figure S9a, Supporting Information) strongly supports that reversible absorption of gases or moisture is responsible for the observed device behavior switches. These results suggest that C-NPG can be doped by molecular dopants, like tetrafluoro-tetracyanoquinodimethane (F$_4$-TCNQ),[39] to modulate the charge transport and further improve device performance. Statistical distribution of the on-current and the on–off ratios of C-NPG FETs measured under vacuum are given in Figure S10, Supporting Information.

In order to obtain a better understanding of the nature of charge transport in C-NPG, we performed electronic structure and transport calculations based on an atomistic mean field Hubbard (MFH) model. **Figure 3**a shows a model of C-NPG in the anti configuration. Here, the unit cell is indicated by the yellow rectangle. The electronic band structure of this material

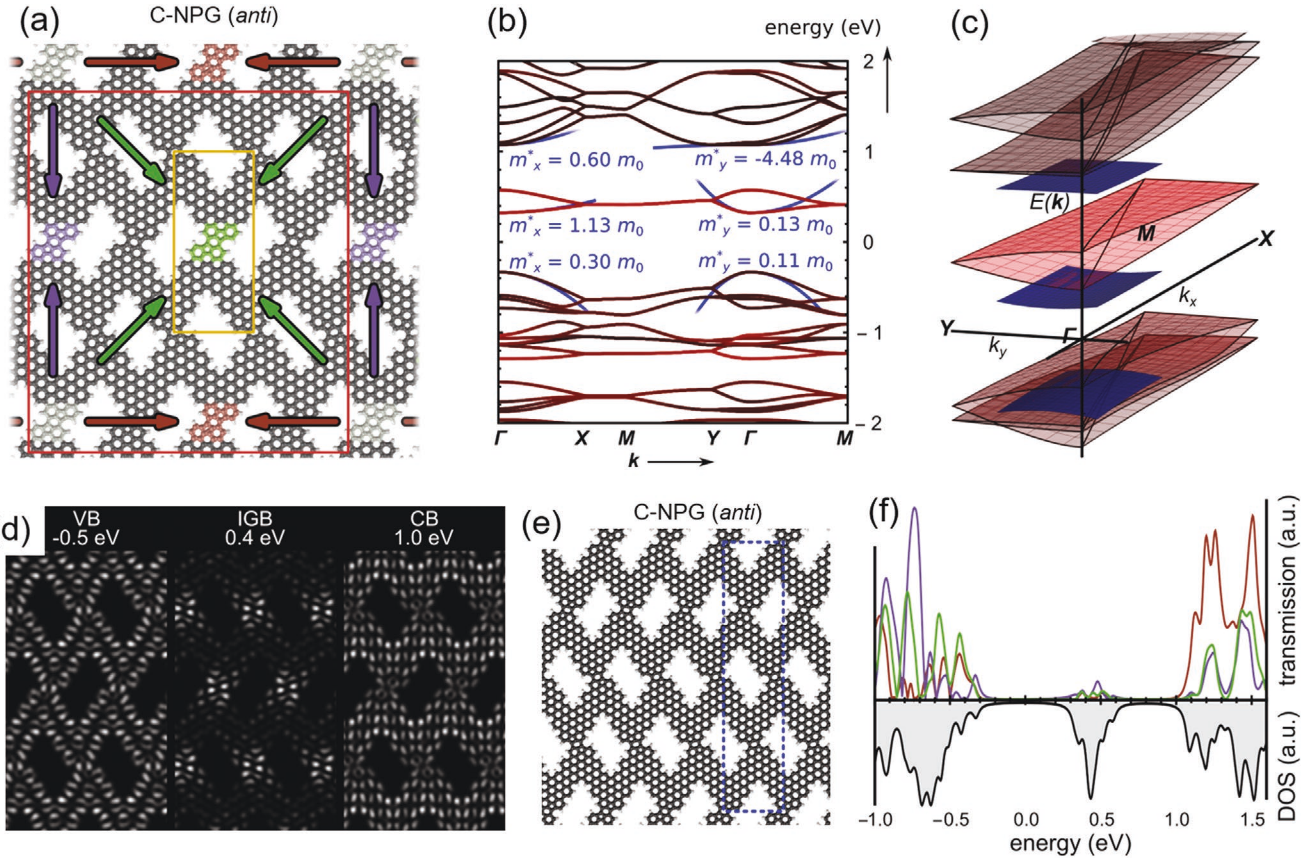

Figure 3. Theoretical analysis of the charge transport in C-NPG. a) Schematic model of the C-NPG (anti), with unit cell indicated by the yellow rectangle. A C-NPG supercell comprising 4 by 2 primitive units is indicated by the red rectangle. Different interfaces are highlighted in gray, brown, purple, and green. Horizontal, vertical, and diagonal transport from the gray interface to the other interfaces is indicated by the brown, purple, and green arrows, respectively. b) Electronic band dispersion of the C-NPG (anti), with parabolic fits (blue) to the band onsets and extracted effective masses indicated. The red shading indicates the wave function localization on the interfaces. c) The same band dispersion as in (b), but rendered in 3D k_x, k_y, E-space. d) Calculated spatial LDOS at the band onsets. e) Structure of C-NPG (syn, anti), with unit cell indicated. f) Transmission (top) and DOS (bottom) as function of energy in the C-NPG supercell of panel (a).

is shown in Figure 3b. The projection of the wave function onto the atoms comprising the rubicene interfaces is indicated by the red shading of the band. In agreement with our previous work, the band structure reveals the presence of a bulk-like valence band (VB) and conduction band (CB) onset, interspersed by a well-demarcated IGB, which has a highly interface-localized character.[6] Interestingly, the band structure consists of pairs of bands that are gapped at low crystal momentum but merge at the Brillouin zone boundary (**X** → **M** → **Y**). This is seen in even more detail when plotting the full, 2D dispersion in 3D k_x, k_y, E-space, as shown in Figure 3c. As explained in Section S2, Supporting Information, this behavior is a necessary consequence of the four equivalent coronene-type subunits in the unit cell in combination with the inversion symmetries present in the unit cell. Also shown in Figure 3b are the anisotropic charge carrier effective masses m^* for all the band onsets, which were calculated by fitting elliptical paraboloids (shown in blue in Figure 3c) to the 2D k_x, k_y, E dispersion at the $\boldsymbol{\Gamma}$ point and applying the quasi-free electron relation $E = E_0 + ½\, \hbar^2\, (k_x^2/m_x^* + k_y^2/m_y^*)$. Figure 3d shows the calculated spatial LDOS at the band onsets, which again showcases the localized character of the IGB but also the fully delocalized nature of the VB onset states, and interface-avoiding nature of the CB onset states. Importantly, when comparing these results with those from our previous work, where the electronic structure was calculated from first principles through density functional theory, it is seen that every detail, including the spatially resolved LDOS and dispersive behavior of all the frontier bands, is reproduced almost perfectly.[6] This validates the atomistic MFH model and lends credibility to the effective masses extracted. Very similar results were obtained for the C-NPG (syn), as shown in Figure S11, Supporting Information. This figure additionally shows the crystal orbitals and (local) density of states (LDOS) for both the syn and anti configurations.

Interestingly, the anisotropic effective masses extracted above reveal a picture that electrons injected into the IGB can conduct well in the fusion direction but are relatively heavy in the growth direction, while the scenario inverts for electrons injected into CB onset states. Holes injected into states near the VB onset have a more isotropic character. The calculated spatial LDOS in Figure 3d supports this intuitive picture by revealing the fully delocalized character of the VB onset states versus the more confined nature of both the IGB states and CB states. Whereas conductance in the IGB states in the growth direction is impeded as the electrons need to "hop around" the pores, the CB states adopt a GNR-like, quasi-1D electronic structure and exhibit very poor coupling in the fusion direction. The picture remains unchanged when a structure is considered having both syn and anti interfaces, as shown in Figure 3e. In fact, the fusion orientation plays almost no role at all in affecting the conductivity, and very similar carrier effective masses are obtained, as shown in Figure S11, Supporting Information.

We also performed transport calculations on the basis of the non-equilibrium Green's function (NEGF) technique, which allows the explicit calculation of the zero-bias transmission as a function of charge carrier energy from one location to another. Figure 3f shows, in brown, purple and green, transmission curves for transport from the interface highlighted in gray in Figure 3a to the interface highlighted in the respective color, and in comparison with the DOS. Given the near-square geometry of the supercell, combined with the periodic nature of the calculation, the transmission curves can be interpreted as representative for horizontal (growth direction), vertical (fusion direction), and diagonal transport, respectively. Comparison of the intensity of the different curves at the band onsets again reveals poor horizontal conductance for the IGB and poor vertical conductance for the CB, in accordance with the anisotropic effective mass model. Since, at the macroscopic level of the devices, transport necessarily involves many steps in both the growth and fusion direction, it may be concluded that electron transport is severely impeded by anisotropy effects, and this is finally corroborated by the near-absence of diagonal transmission in Figure 3f. This is in contrast with the relatively isotropic hole conductance at the VB onset. More calculations (see Section S3, Supporting Information for the details) were performed on finite-sized patches to investigate the effect of unfused segments and defects, as shown in Figure S12, Supporting Information, which additionally showcase the fragility of the IGB while the VB and CB onsets are more robust. We summarize this section by concluding that electron transport in C-NPG is likely to suffer from anisotropy and defects, and may therefore attain a diffusive nature, while hole conductance could be more efficient. Indeed, when taking the experimental results into consideration, the relatively low on-current—which is still comparable with most of bottom-up synthesized GNR FETs[10,13,15–21,40] is suggestive of diffusive transport. This can now be understood to happen due to the sensitivity of the charge transport to structural imperfections, which in turn is a consequence of the high inherent conductance anisotropy of the C-NPG. Besides the structural imperfections, tunneling through a Schottky barrier (SB) at the contacts[12,13] also limits the performance of the devices, which is also commonly seen in bottom-up GNR FETs.[8] The presence of the SB at the Pd-C-NPG interface is evident by non-linear behavior at low bias in the I_d–V_d characteristics, as shown in the inset of Figure 2f. The work-function engineering of the contact metal or doping of the contact could potentially eliminate SB effects.[8]

3. Conclusion

In conclusion, we have demonstrated successful fabrication of short-channel FETs with bottom-up synthesized C-NPG with excellent switching behavior with on–off ratios exceeding 10^4, which makes them potentially promising for logic applications. Even though C-NPG is an NPG, consisting of C-GNRs, this performance is superior to that of bulk graphene,[19] top-down nanoporous graphenes,[2] and C-GNRs.[20–22] This shows that the bottom-up method gives access to a superior NPG material as a result of the control over the geometry and electronic properties at the atomic level. C-NPG FETs exhibit a predominant p-type charge transport behavior in air while the devices under vacuum are converted to n-type transistor. The recovery of p-type transport behavior after air exposure indicates that reversible absorption of gases or moisture is responsible for the device behavior switches. Owing to its high sensitivity to molecular absorbates, C-NPG might be used in ultra-sensitive chemical and biological sensors. We have also demonstrated versatility of Raman spectroscopy as a high-throughput ex situ characterization tool for C-NPG after growth, upon air exposure, and after device integration to monitor its structural quality and stability. The theoretical charge transport analysis reveals strong conductance anisotropy effects in C-NPG, which is fundamentally a consequence of the well-defined geometry at the atomic level afforded by the bottom-up synthesis and is therefore difficult to achieve through top-down methods like lithographic etching. Unfortunately, in the present study, this anisotropy only serves to reduce the on-current in C-NPG devices since the sensitivity of charge transport to structural imperfections results in significant scattering that prevents us from obtaining ballistic conductance. However, the huge increase in on–off ratio in going from the low-quality sample to the high-quality sample clearly shows that structural perfection plays an enormously important role in the charge transport and it is well conceivable that with further optimization, ballistic conductance, and conduction anisotropy effects may be within experimental reach in the near future.

4. Experimental Section

Growth and STM Imaging of C-NPG: Atomically clean Au(111) surfaces (≈5 × 5 mm Au(111) thin films on mica) were prepared through repeated cycles of argon ion (Ar^+) sputtering and annealing under ultra-high vacuum (UHV). Molecular precursors **1** (methyl cross-linking handle) and **2** (fluorene cross-linking handle) were deposited by sublimation using a home-built Knudsen cell evaporator at a crucible temperature of $T = 200$ °C. Polymer growth was performed by keeping the substrate at a temperature of $T_1 = 220$ °C while depositing the precursor of choice over the course of $t = 45$ min. Graphitization (CDH and cross-dehydrogenative coupling) was induced by heating the sample to $T_2 = 430$ °C for $t = 10$ min. All STM experiments were carried out using a commercial Createc LT-STM held at $T = 4.5$ K using platinum–iridium tips. Image processing of the STM scans was performed with WSxM.

Preparation of HfO_2 Local Back Gates: ≈100 nm SiO_2 was grown on 150 mm Si wafers using dry oxidation. The local back gates were defined by sputtering of ≈8 nm W and subsequent wet-etch. The ≈5.5 nm HfO_2 (Equivalent oxide thickness, EOT = ≈1.8 nm, dielectric capacitance, $C_{ox} \approx 19.0$ µF cm^{-2}) was grown in an ALD system (Oxford, FlexAl Plasma ALD) at 135 °C. Alignment markers and large pads for electrical probing were patterned using standard photolithography followed by lift-off of ≈3 nm Cr and ≈25 nm Pt. The wafer was then diced, and individual chips were used for further device processing.

Transfer of C-NPG and Patterning of Pd Electrodes: C-NPG/Au/mica was floated in 38% HCl in water, which caused the mica to delaminate with C-NPG/Au film floating on the surface of the acid. The floating film was picked up with the target substrate, with C-NPG facing the dielectric surface followed by a hot plate baking at 100 °C for 10 min. Subsequent gold etching in a potassium iodide based gold etchant solution (potassium iodine) yielded C-NPG on the target substrate. After the transfer, poly(methyl methacrylate) (molecular weight 950 kDa) was spun on the chips at 4000 rpm followed by a 10 min bake at 180 °C. Next, the drain and source electrodes (≈200 nm wide, ≈20 nm gaps) were patterned using a JEOL 6300-FS 100 kV EBL system and subsequently developed in 3:1 IPA-MIBK at 5 °C for 90 s. Finally, ≈12 nm Pd was deposited using e-beam evaporation (Kurt J. Lesker), and lift-off was completed in a Remover PG at 80 °C.

Raman Spectroscopy Characterization: Raman characterization of C-NPG films was performed using a Horiba Jobin Yvon LabRAM ARAMIS Raman microscope using a 532 nm laser with <10 mW power and a 100× objective lens, resulting in a laser spot size of <1 µm. No thermal effects were observed under these measurement conditions, and at least three spectra from different points were collected for each sample.

AFM Imaging: The surface topography of the samples was obtained by a Bruker Dimension Icon AFM with ScanAsyst imaging and NanoScope software, operating in tapping mode at ambient conditions, using a Si probe (Bruker, RTESPA-300) with a tip radius of ≈8 nm (force constant: ≈40 N m^{-1}, resonance frequency: ≈300 kHz). The height diagrams were recorded with scan sizes of 1 µm and scan speeds of 0.6 Hz (512 × 512 points). Nanoscope analysis software was used for AFM data analysis.

Electrical Characterization: The electrical characterization of C-NPG FETs was performed in the Lakeshore CPX-HF probe with the Agilent 4155C semiconductor parameter analyzer and EasyEXPERT software at room temperature in air and vacuum ($\approx 1 \times 10^{-4}$ torr).

Calculations: Electronic structure calculations were performed with MathemaTB[41] using an atomistic MFH model applied to a basis of p_z-orbitals on the carbon atoms. In the implementation, the Schrödinger equation was solved in a self-consistent field procedure to generate the self-consistent spin Hamiltonians, from which the electronic dispersion and wave functions were extracted. A nearest-neighbor parametrization was used with $t = -2.7$ eV and $\varepsilon_0 = 0$. Increased hopping between carbon atoms at the edges was taken into account by setting $t_{\text{edge}} = 1.12\ t$ whenever the carbon atoms were each bonded to a hydrogen atom.[42,43] A Hubbard parameter $U = 3.5$ eV was used to account for electron–electron interaction.[44] In the implementation of the NEGF procedure, the self-consistent spin Hamiltonians from the MFH model were used as the system was connected to leads through coupling matrices $\boldsymbol{\Gamma}_\text{A}$, $\boldsymbol{\Gamma}_\text{B}$, $\boldsymbol{\Gamma}_\text{C}$, and $\boldsymbol{\Gamma}_\text{D}$, representing the respective rubicene interfaces. These were defined in a wide-band limit (WBL) as $\boldsymbol{\Gamma}_{mn} = (1\ \text{eV})\ \delta_{mn}$. The zero-bias transmission was calculated from the trace of the transmission matrix, which was computed from the Green's function matrices, which in turn were constructed from the spin Hamiltonian and coupling matrices (see Section S1, Supporting Information for more details)

Supporting Information

Supporting Information is available from the Wiley Online Library or from the author.

Acknowledgements

Z.M. and P.H.J. contributed equally to this work. This work was supported in part by the Office of Naval Research (ONR) MURI Program N00014-16-1-2921, the National Science Foundation (NSF) Center for Energy Efficient Electronics Science (E3S), and the NSF under award DMR-1839098. Raman spectroscopy characterization, charge transport measurements, and atomic layer deposition were performed at the Molecular Foundry at Lawrence Berkeley National Laboratory (LBNL), supported by the Office of Science, Office of Basic Energy Sciences, of the U.S. Department of Energy (DOE) under contract no. DE-AC02-05CH11231. Device fabrication was performed at the Stanford Nano Shared Facilities (SNSF) at Stanford University, supported by the NSF under award ECCS-1542152. P.H.J. acknowledges funding from the Dutch Research Council through Rubicon award 019.182EN.018. Part of this work was also performed at the Marvell Nanofabrication Laboratory at the University of California, Berkeley. The authors thank N. Gupta and A. Javey for access to atomic force microscopy at the University of California, Berkeley. The authors also thank E. Chan, S. Dhuey, S. Shelton, T. Mattox, and A. Schwartzberg for laboratory and instrument access in the Molecular Foundry at LBNL.

Conflict of Interest

The authors declare no conflict of interest.

Data Availability Statement

The data that support the findings of this study are available from the corresponding author upon reasonable request.

Keywords

bottom-up on-surface synthesis, electronic structure, field-effect transistors, graphene nanoribbons, nanoelectronics, nanoporous graphene, Raman spectroscopy, transport calculations

Received: April 22, 2021
Revised: July 20, 2021
Published online: August 21, 2021

---

[1] X. Liang, Y.-S. Jung, S. Wu, A. Ismach, D. L. Olynick, S. Cabrini, J. Bokor, *Nano Lett.* **2010**, *10*, 2454.
[2] J. Bai, X. Zhong, S. Jiang, Y. Huang, X. Duan, *Nat. Nanotechnol.* **2010**, *5*, 190.
[3] W. Yuan, J. Chen, G. Shi, *Mater. Today* **2014**, *17*, 77.
[4] J. Cai, P. Ruffieux, R. Jaafar, M. Bieri, T. Braun, S. Blankenburg, M. Muoth, A. P. Seitsonen, M. Saleh, X. Feng, K. Müllen, R. Fasel, *Nature* **2010**, *466*, 470.
[5] Z. Chen, A. Narita, K. Müllen, *Adv. Mater.* **2020**, *32*, 2001893.
[6] P. H. Jacobse, R. D. McCurdy, J. Jiang, D. J. Rizzo, G. Veber, P. Butler, R. Zuzak, S. G. Louie, F. R. Fischer, M. F. Crommie, *J. Am. Chem. Soc.* **2020**, *142*, 13507.
[7] C. Moreno, M. Vilas-Varela, B. Kretz, A. Garcia-Lekue, M. V. Costache, M. Paradinas, M. Panighe, G. Ceballos, S. O. Valenzuela, D. Peña, A. Mugarza, *Science* **2018**, *360*, 199.
[8] V. Saraswat, R. M. Jacobberger, M. S. Arnold, *ACS Nano* **2021**, *15*, 3674.
[9] G. Borin, A. Fairbrother, L. Rotach, M. Bayle, M. Paillet, L. Liang, V. Meunier, R. Hauert, T. Dumslaff, A. Narita, K. Müllen, H. Sahabudeen, R. Berger, X. Feng, R. Fasel, P. Ruffieux, *ACS Appl. Nano Mater.* **2019**, *2*, 2184.
[10] Q. Sun, O. Gröning, J. Overbeck, O. Braun, M. L. Perrin, G. B. Barin, M. E. Abbassi, K. Eimre, E. Ditler, C. Daniels, V. Meunier, C. A. Pignedoli, M. Calame, R. Fasel, P. Ruffieux, *Adv. Mater.* **2020**, *32*, 1906054.
[11] Z. Mutlu, J. P. Llinas, P. H. Jacobse, I. Piskun, R. Blackwell, M. F. Crommie, F. R. Fischer, J. Bokor, *ACS Nano* **2021**, *15*, 2635.
[12] J. P. Llinas, A. Fairbrother, G. B. Barin, W. Shi, K. Lee, S. Wu, B. Y. Choi, R. Braganza, J. Lear, N. Kau, W. Choi, C. Chen, Z. Pedramrazi, T. Dumslaff, A. Narita, X. Feng, K. Müllen, F. Fischer,

A. Zettl, P. Ruffieux, E. Yablonovitch, M. Crommie, R. Fasel, J. Bokor, *Nat. Commun.* **2017**, *8*, 633.
[13] P. B. Bennett, Z. Pedramrazi, A. Madani, Y.-C. Chen, D. G. de Oteyza, C. Chen, F. R. Fischer, M. F. Crommie, J. Bokor, *Appl. Phys. Lett.* **2013**, *103*, 253114.
[14] N. Richter, Z. Chen, A. Tries, T. Prechtl, A. Narita, K. Müllen, K. Asadi, M. Bonn, M. Kläui, *Sci. Rep.* **2020**, *10*, 1988.
[15] A. Fairbrother, J.-R. Sanchez-Valencia, B. Lauber, I. Shorubalko, P. Ruffieux, T. Hintermannc, R. Fasel, *Nanoscale* **2017**, *9*, 2785.
[16] L. Martini, Z. Chen, N. Mishra, G. B. Barin, P. Fantuzzi, P. Ruffieux, R. Fasel, X. Feng, A. Narita, C. Coletti, K. Müllen, *Carbon* **2019**, *146*, 36.
[17] M. El Abbassi, M. L. Perrin, G. B. Barin, S. Sangtarash, J. Overbeck, O. Braun, C. J. Lambert, Q. Sun, T. Prechtl, A. Narita, K. Müllen, P. Ruffieux, H. Sadeghi, R. Fasel, M. Calame, *ACS Nano* **2020**, *14*, 5754.
[18] V. Passi, A. Gahoi, B. V. Senkovskiy, D. Haberer, F. R. Fischer, A. Grüneis, M. C. Lemme, *ACS Appl. Mater. Interfaces* **2018**, *10*, 9900.
[19] F. Schwierz, *Nat. Nanotechnol.* **2010**, *5*, 487.
[20] X. Liu, G. Li, A. Lipatov, T. Sun, M. Mehdi Pour, N. R. Aluru, J. W. Lyding, A. Sinitskii, *Nano Res.* **2020**, *13*, 1722.
[21] M. Shekhirev, T. H. Vo, M. M. Pour, A. Lipatov, S. Munukutla, J. W. Lyding, A. Sinitskii, *ACS Appl. Mater. Interfaces* **2017**, *9*, 693.
[22] Z. Chen, W. Zhang, C.-A. Palma, A. L. Rizzini, B. Liu, A. Abbas, N. Richter, L. Martini, X.-Y. Wang, N. Cavani, H. Lu, N. Mishra, C. Coletti, R. Berger, F. Klappenberger, M. Kläui, A. Candini, M. Affronte, C. Zhou, V. De Renzi, U. d. Pennino, J. V. Barth, H. J. Räder, A. Narit, X. Feng, K. Müllen, *J. Am. Chem. Soc.* **2016**, *138*, 15488.
[23] L. M. Malard, M. A. Pimenta, G. Dresselhaus, M. S. Dresselhaus, *Phys. Rep.* **2009**, *473*, 51.
[24] A. C. Ferrari, J. C. Meyer, V. Scardaci, C. Casiraghi, M. Lazzeri, F. Mauri, S. Piscanec, D. Jiang, K. S. Novoselov, S. Roth, A. K. Geim, *Phys. Rev. Lett.* **2006**, *97*, 187401.
[25] M. S. Dresselhaus, G. Dresselhaus, R. Saito, A. Jorio, *Phys. Rep.* **2005**, *409*, 47.
[26] A. C. Ferrari, D. M. Basko, *Nat. Nanotechnol.* **2013**, *8*, 235.
[27] J. D. Teeter, P. S. Costa, P. Zahl, T. H. Vo, M. Shekhirev, W. Xu, X. C. Zeng, A. Enders, A. Sinitskii, *Nanoscale* **2017**, *9*, 18835.
[28] P. S. Costa, J. D. Teeter, A. Enders, A. Sinitskii, *Carbon* **2018**, *134*, 310.
[29] T. H. Vo, M. Shekhirev, D. A. Kunkel, F. Orange, M. J.-F. Guinel, A. Endersbe, A. Sinitskii, *Chem. Commun.* **2014**, *50*, 4172.
[30] T. H. Vo, M. Shekhirev, D. A. Kunkel, M. D. Morton, E. Berglund, L. Kong, P. M. Wilson, P. A. Dowben, A. Enders, A. Sinitskii, *Nat. Commun.* **2014**, *5*, 3189.
[31] M. M. Pour, A. Lashkov, A. Radocea, X. Liu, T. Sun, A. Lipatov, R. A. Korlacki, M. Shekhirev, N. R. Aluru, J. W. Lyding, V. Sysoev, A. Sinitskii, *Nat. Commun.* **2017**, *8*, 820.
[32] T. H. Vo, M. Shekhirev, A. Lipatov, R. A. Korlacki, A. Sinitskii, *Faraday Discuss.* **2014**, *173*, 105.
[33] R. Sainz, M. d. Pozo, M. Vilas-Varela, J. Castro-Esteban, M. P. Corral, L. Vázquez, E. Blanco, D. Peña, J. A. Martín-Gago, G. J. Ellis, M. D. Petit-Domínguez, C. Quintana, E. Casero, *Sci. Rep.* **2020**, *10*, 14614.
[34] C. Ma, Z. Xiao, A. A. Puretzky, A. P. Baddorf, W. Lu, K. Hong, J. Bernholc, A.-P. Li, *Phys. Rev. Mater.* **2018**, *2*, 014006.
[35] G. Pitner, G. Hills, J. P. Llinas, K.-M. Persson, R. Park, J. Bokor, S. Mitra, H.-S. P. Wong, *Nano Lett.* **2019**, *19*, 1083.
[36] B. V. Senkovskiy, M. P. Orcid, S. K. Alavi, A. Bliesener, J. Zhu, S. Michel, A. V. Fedorov, R. German, D. Hertel, D. Haberer, L. Petaccia, F. R. Fischer, K. Meerholz, P. H. M. van Loosdrecht, K. Lindfor, A. Grüneis, *Nano Lett.* **2017**, *17*, 4029.
[37] Q. Qian, G. Li, Y. Jin, J. Liu, Y. Zou, K. Jiang, S. Fan, Q. Li, *ACS Nano* **2014**, *8*, 9597.
[38] J. Liu, Y. Wang, X. Xiao, K. Zhang, N. Guo, Y. Jia, S. Zhou, Y. Wu, Q. Li, L. Xiao, *Nanoscale Res. Lett.* **2018**, *13*, 291.
[39] L. Yu, A. Zubair, E. J. G. Santos, X. Zhang, Y. Lin, Y. Zhang, T. Palacios, *Nano Lett.* **2015**, *15*, 4928.
[40] M. Ohtomo, Y. Sekine, H. Hibino, H. Yamamoto, *Appl. Phys. Lett.* **2018**, *112*, 021602.
[41] P. H. Jacobse, *Comput. Phys. Commun.* **2019**, *244*, 392.
[42] Y. W. Son, M. L. Cohen, S. G. Louie, *Phys. Rev. Lett.* **2006**, *97*, 216803.
[43] S. Mishra, D. Beyer, K. Eimre, R. Ortiz, J. Fernández-Rossier, R. Berger, O. Gröning, C. A. Pignedoli, R. Fasel, X. Feng, P. Ruffieux, *Angew. Chem., Int. Ed.* **2020**, *59*, 12041.
[44] Y. Zheng, C. Li, C. Xu, D. Beyer, X. Yue, Y. Zhao, G. Wang, D. Guan, Y. Li, H. Zheng, C. Liu, J. Liu, X. Wang, W. Luo, X. Feng, S. Wang, J. Jia, *Nat. Commun.* **2020**, *11*, 6076.